Journal of
Synchrotron
Radiation

ISSN 0909-0495

Received 28 May 2005
Accepted 8 July 2005

Structural changes induced by lattice–electron interactions: SiO_2 stishovite and $FeTiO_3$ ilmenite

Takamitsu Yamanaka

Department of Earth and Space Science, Graduate School of Science, Osaka University, Machikaneyama, Toyonaka, Osaka 560-0043, Japan. E-mail: yamanaka@hpc.cmc.osaka-u.ac.jp

The bright source and highly collimated beam of synchrotron radiation offers many advantages for single-crystal structure analysis under non-ambient conditions. The structure changes induced by the lattice–electron interaction under high pressure have been investigated using a diamond anvil pressure cell. The pressure dependence of electron density distributions around atoms is elucidated by a single-crystal diffraction study using deformation electron density analysis and the maximum entropy method. In order to understand the bonding electrons under pressure, diffraction intensity measurements of $FeTiO_3$ ilmenite and γ-SiO_2 stishovite single crystals at high pressures were made using synchrotron radiation. Both diffraction studies describe the electron density distribution including bonding electrons and provide the effective charge of the cations. In both cases the valence electrons are more localized around the cations with increasing pressure. This is consistent with molecular orbital calculations, proving that the bonding electron density becomes smaller with pressure. The thermal displacement parameters of both samples are reduced with increasing pressure.

Keywords: high-pressure diffraction; single-crystal structure analysis; electron density distribution; γ-SiO_2; stishovite; $FeTiO_3$ ilmenite.

1. Introduction

Studies of the changes in crystal structures and physical properties of crystals under non-ambient conditions have contributed significantly to our understanding of materials such as solid ionics, ferroelectrics, ferromagnetics and minerals forming Earth and other planet interiors. Various solid-state phenomena induced or strongly affected by compression are phase transformation, lattice deformation, cation ordering, decomposition, amorphization and solid-state reactions. Since miniature diamond-anvil pressure cell (DAC) and multi-anvil high-pressure apparatus were developed, numerous structural studies under high pressure have been carried out with X-ray diffraction, as well as non-diffraction techniques such as Raman and infrared spectroscopy, using single-crystal or polycrystalline samples, and often combining compression with heating (electric resistance heaters or lasers) or cooling (using cryostats).

Phase transitions under compression may occur owing to lattice instability, including electronic state change and magnetic spin ordering, and can be investigated by means of X-ray techniques, utilizing diffraction, absorption or resonance phenomena. Numerous reports regarding phase transformations under static high-pressure conditions have been published during the last 20 years.

The present investigation aims to clarify the structure changes induced by phonon–electron interaction under high pressure. The pressure dependence of electron density distributions around atoms is elucidated by a single-crystal diffraction study using synchrotron radiation and the maximum entropy method (MEM).

2. Pressure effects on crystal structure

A macroscopic system under pressure can be described quantitatively by statistical thermodynamics. Pressure P, volume V and temperature T are not all individually independent but are related to each other by an equation of state. The spatial and time average of atomic positions in a crystal can be expressed with the aid of statistical mechanics.

The virial theorem gives a view of the compression mechanism of substances under pressure. The external pressure $P_{\rm ext}$ provided by pressure generation systems such as DAC and multi-anvil high-pressure apparatus can be expressed by the following equation,

$$P_{\rm ext} = (Nk_{\rm B}T/V) - (1/3V)\Big\langle \sum_{j=1}^{N}\sum_{j>1}^{N}\big(-\partial\psi_{ij}/\partial r_{ij}\big)\,\mathbf{r}_{ij}\Big\rangle$$
$$= (Nk_{\rm B}T/V) - (1/3V)\Big\langle \sum_{j=1}^{N}\sum_{j>1}^{N}\mathbf{F}_{ij}\cdot\mathbf{r}_{ij}\Big\rangle, \qquad (1)$$

where V is the cell volume, N is the number of particles, ψ_{ij} is the internal potential between atoms i and j, $\mathbf{r}_{ij}$ is the interatomic distance between atoms i and j, and $\mathbf{F}_{ij}$ $(= -\partial\psi_{ij}/\partial r_{ij})$ is the interatomic force acting between atoms i and j.

Equation (1) implies that the external pressure can be represented by $\sum_{j=1}^{N}\sum_{j>1}^{N}\mathbf{F}_{ij}\cdot\mathbf{r}_{ij}$, and that the inner pressure of the compressed substance is in equilibrium with the external pressure.

Structure analysis under high pressure evaluates $\mathbf{r}_{ij}$ as a function of pressure. Information about the positions of atoms can be obtained through analysis of peak intensities measured in X-ray or neutron diffraction experiments. The interatomic forces $\mathbf{F}_{ij}$ can be determined by a lattice dynamical experiment, such as Raman and infrared spectroscopy under high pressure. Electron spectroscopy for chemical analysis and photoelectron spectroscopy are also candidates for providing interatomic force information. The pressure-induced change of volume V results from the energy change $\mathbf{F}_{ij}\cdot\mathbf{r}_{ij}$ with pressure.

3. Structure study using synchrotron radiation

Since synchrotron radiation became available, structural studies have been more intensively performed under high pressure. Several beamlines have been designed especially for high-pressure studies by means of XAFS, single-crystal and powder diffraction (also with laser heating or cryogenic cooling), inelastic scattering, and infrared and X-ray Mössbauer spectroscopy. High-pressure diffraction studies encounter new difficulties for *in situ* observations compared with ambient experiments. However, synchrotron radiation has excellent beam characteristics for high-pressure diffraction studies. The brilliance of the synchrotron radiation emitted from a bending magnet is about 10^{12} photons s^{-1} mm^{-2} $mrad^{-2}$ (0.1% bandwidth)$^{-1}$, which is about 10^4 times larger than that of a conventional rotating-anode X-ray generator [10^8 photons s^{-1} mm^{-2} $mrad^{-2}$ (0.1% bandwidth)$^{-1}$]. Insertion devices such as wigglers or undulators further enhance the source intensity. The high source intensity of synchrotron radiation has the following advantages: large transmittance for anvil or window in the X-ray path, high signal-to-noise (S/N) ratio of the diffraction intensity, detection of weak diffraction peaks, narrow peak profiles and a short measurement time. Synchrotron radiation, having a tunable energy, permits the choice of optimum incident wavelength for a high-pressure diffraction study. Since the small aperture angle of a DAC or multi-anvil pressure apparatus gives a limited diffraction angle, a short wavelength has the advantage of accessing a large portion of reciprocal space, providing a large Q-value [$= (2\sin\theta/\lambda)^2$].

In the present experiment, the synchrotron radiation beam with 8 GeV and 100 mA of beam current at SPring-8 provides a critical energy of about 30 keV emitted from the bending magnet, where the maximum photon count is expected in a continuous energy distribution. The beam was focused by a Pt-coated mirror and passed as an incident beam through the evacuated guide pipe, which significantly reduced the background intensities. A Huber Eulerian cradle (512.1) seven-circle goniometer and scintillation counter in BL02B1 were utilized, as depicted in Fig. 1. A collimator with a diameter of 100 µm was adopted, because the gasket hole was 200 µm and the sample size was several tens of micrometres across. A receiving slit angle of 1° was used. The evacuated collimator and guide pipe were placed very close to the DAC. The incident beam was monochromated to λ = 0.40772 Å (E = 30.388 keV) by a Si(111) double-crystal monochromator. As discussed above, the short wavelength enables one to observe higher-order reflections, resulting in an increasing total number of observations that is four times larger than from a laboratory source. A further increase in the number of observed reflections was obtained by using widely opened and transparent diamond windows, permitting access to reflections with $2\theta < 70°$, with maximum Q = 5.1303 (d = 0.44150 Å). The increased number of observations enables a more precise discussion of the electron densities and atomic thermal displacement as a function of pressure.

4. DAC for single-crystal structure analysis

Various new designs and modifications of the original DAC have been introduced during the last three decades. Special designs optimized for powder diffraction experiments at ultrahigh pressures have made it possible to obtain structural information at over 300 GPa (Mao *et al.*, 1978). Single-crystal

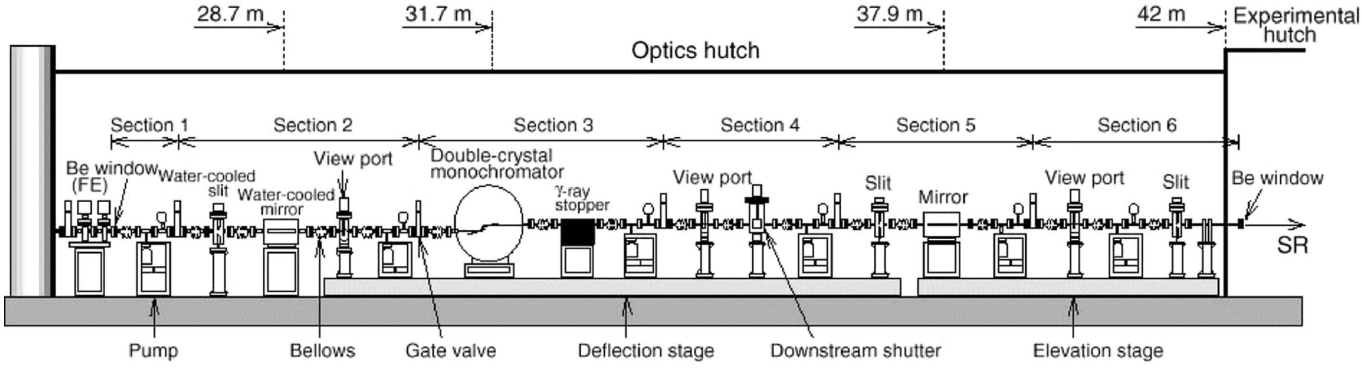

Figure 1
Schematic drawing of the BL02B1 beamline facility at SPring-8.

structure analysis under pressure, on the other hand, introduces a number of additional difficulties, including determining accurate intensities, hydrostaticity, a large blind region owing to the pressure cell, X-ray absorption and limitation of compression. Structure determinations reported in the literature are studies on ruby (Al_2O_3) to 31 GPa (Kim-Zajonz *et al.*, 1998) and pyrope ($Mg_3Al_2Si_3O_{12}$) to 33 GPa (Zhang *et al.*, 1998). The DAC with diamond backing plates solves most of the above problems intrinsic to single-crystal experiments and enables us to discuss the electron density distribution under pressures up to 50 GPa (Yamanaka *et al.*, 2001).

Generally, beryllium windows have been used as backing plates for single-crystal diffraction measurement. However, the polycrystalline backing plates generate many broad, strong and spotty powder rings. We have tried to find a much more efficient window material instead of beryllium.

Our DAC consists of large single-crystal diamond plates supporting diamond anvils. The (100) plates of about two carats with a size of 6 mm × 6 mm and thickness 2 mm are directly fixed onto the (100) table plane of diamond anvils, as shown in Fig. 2. The diamond plate windows have quite a small absorption effect on the intensities of the incident and diffracted beams.

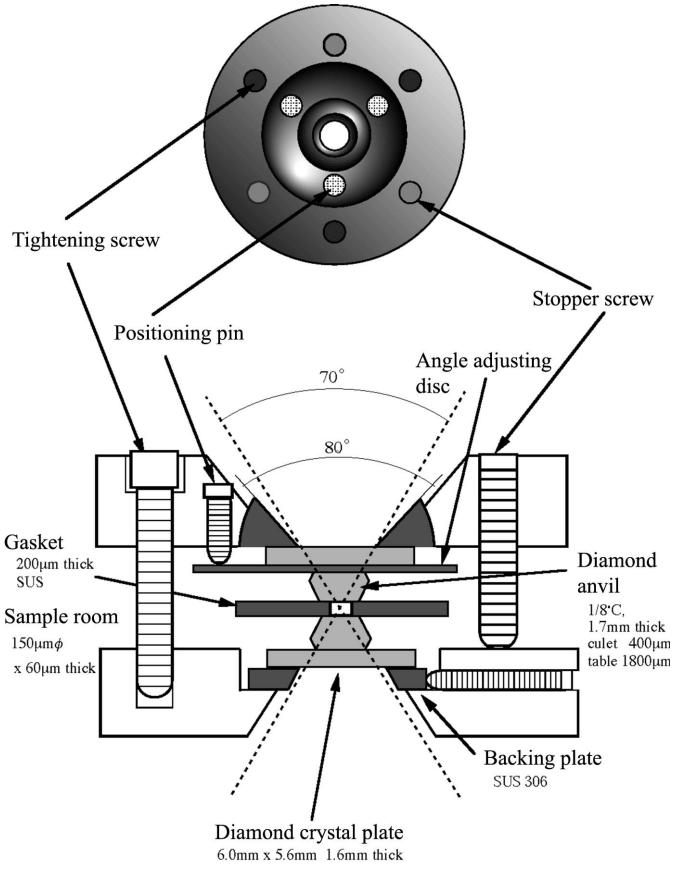

Figure 2
The DAC used for the X-ray single-crystal diffraction study. Large single-crystal diamond plates were used as the windows. 1/8-Carat brilliant-cut diamond anvils were applied. Both diamond plates and anvils were directly fixed onto the (100) plane with a topotactic relation.

Beryllium plates or disc windows cannot be used for diffraction studies under pressures higher than 20 GPa because of their softness. Diamond plate windows permit diffraction studies to over 50 GPa in the case of a diamond anvil with table and culet planes of 1 mm and 400 μm in diameter. In general, steel backing plates and angle positioning discs (or anvil holder) create a large blind region, but large diamond plates allow a wide window with a maximum diffraction angle of 70°.

5. Single-crystal structure refinement under non-ambient pressure

Unit-cell parameters of samples under pressure were determined by peak profile fitting followed by peak refinement applying 2θ values of 25 independent reflections falling within the range $30^\circ < 2\theta < 40^\circ$. Based on the unit-cell volume calculated from the observed cell constants, the volume change V/V_0 with pressure can be followed, and the isothermal bulk modulus K and its pressure derivative dK/dP can be determined by fitting a Birch-Murghanan equation of sate to the $V(p)$ data.

Peak intensity measurements were made using a 2θ scan with a speed of 2° min^{-1} and scanning width of $1.5^\circ + 0.5^\circ \tan\theta$. The observed structure factor $F_o(hkl)$ of reflection hkl was obtained from the observed diffraction intensity $I_{obs}(hkl)$. The observed intensities I_{obs} were corrected for Lorentz and polarization effects Lp and absorption $A(\theta)$.

Reflections having $|F_o| > 3\sigma|F_o|$ within $0.1\ \text{Å}^{-1} < \sin\theta/\lambda < 1.32\ \text{Å}^{-1}$ were used for the ordinary structure refinement. Atomic scattering factors for neutral or ionized atoms were taken from *International Tables for X-ray Crystallography* (1974). The structure refinement using each data set has been conducted by the full matrix least-squares program *RADY* (Sasaki & Tsukimura, 1987). The reliability factor (R) of the least-squares refinement is defined as

$$\begin{aligned} R &= \sum(||F_{obs}| - |F_{cal}||)/\sum|F_{obs}|, \\ wR &= \sum w(||F_{obs}| - |F_{cal}||)/\sum w|F_{obs}| \\ R &= [\sum(||F_{obs}| - |F_{cal}||^2)/\sum|F_{obs}|^2]^{1/2} \\ wR &= [w\sum(||F_{obs}| - |F_{cal}||^2)/\sum w|F_{obs}|^2]^{1/2}, \end{aligned} \tag{2}$$

where $w = 1/\sigma^2(|F_{obs}|)$.

6. Charge density distribution as a function of pressure

After the conventional structure refinement mentioned above, electron density analysis was performed by monopole refinement introducing the κ-parameter in the atomic scattering factors. According to the pseudo-potential model, the core electrons are frozen by bonding effects, while the valence electrons, being weakly bound to the nuclei, form clouds that fill the surrounding coordination. The interactions of the valence and core electrons are relatively weak. Accordingly they are more sensitive to the interatomic potential affected by the coordination of the adjacent atoms. Since the defor-

mation from the spherical electron distribution is assumed to be very small except for excitation of *d* electrons, a monopole refinement was applied instead of the multipole deformation density. The κ-parameter (Coppens *et al.*, 1979; van der Wal & Stewart, 1984) was applied in the atomic scattering factor, which is an indicator of the radial distributions of electrons. The atomic scattering factor $f(s)$ was modified from a Hartree–Fock approximation based on the isolated-atom model. The perturbed valence electron density is

$$f(s/2) = \sum\left[P_{j,\text{core}} f_{j,\text{core}}(s/2) + P_{j,\text{valence}} f_{j,\text{valence}}(\kappa_j, s/2) + f_j' + if_j''\right]. \quad (3)$$

The valence scattering of the perturbed atom at $s/2$ ($= \sin\theta/2\lambda$) is given by

$$f_{\text{M-core}}(\kappa_j, s/2) = f_{j,\text{M-core(free atom)}}(\sin\theta/\lambda)(1/\kappa_j). \quad (4)$$

A localized electron distribution as indicated by $\kappa = 1.0$ implies more ionic character in the bonding nature. The detailed formalization is discussed by Yamanaka *et al.* (2000). The valence charge of a cation was introduced by a population parameter. Effective charge was determined from the κ-parameter of the oxygen atomic scattering factor. The parameters P and κ could be simultaneously refined as variable parameters. The κ-parameter and population parameter were obtained by minimization of the reliability factor R [equation (2)].

The valence electrons around the atomic position and the bonding electron distribution cannot be separately evaluated by structure refinement. The covalency of the bond character is estimated from the effective charge. The difference Fourier synthesis and the population parameter show an electron deformation density. The effective charge q is obtained by the spatial integration of the difference electron density by

$$q = -\int \Delta\rho(r)\,\mathrm{d}r = -4\pi \int r^2 \rho(r)\,\mathrm{d}r. \quad (5)$$

The structure factor of the unit cell is defined by the Fourier transform of the electron density of $\rho(\mathbf{r})$.

On the contrary, $\rho(\mathbf{r})$ is an inverse Fourier transform of the structure factor $F(\mathbf{h})$,

$$\rho(\mathbf{r}) = \int_{\text{unit cell}} F(\mathbf{h}) \exp(2\pi i\, \mathbf{h}\cdot\mathbf{r})\,\mathrm{d}v^*, \quad (6)$$

where $\mathrm{d}v^*$ is defined by the spatial volume.

Hence electron density in the crystal can be calculated from $F_{\text{obs}}(\mathbf{h})$. However, $F_{\text{obs}}(\mathbf{h})$ is not a continuous function in the reciprocal space, but rather has an effective value only around the reciprocal point of *hkl*. It becomes zero outside the reciprocal nodes. Therefore equation (6) is replaced by the following expression, in which summation replaces integration,

$$\rho(x, y, z) = \frac{1}{V}\sum_h \sum_k \sum_l F(hkl) \exp[-2\pi i(hx + ky + lz)]. \quad (7)$$

The difference Fourier synthesis $[F_{\text{obs}}(hkl) - F_{\text{cal}}(hkl)]$ brings a difference electron density $\Delta\rho$ between the observed $\rho_{\text{obs}}(x, y, z)$ and calculated $\rho_{\text{cal}}(x, y, z)$,

$$\Delta\rho(x, y, z) = \frac{1}{V}\sum_h \sum_k \sum_l \left[F_{\text{obs}}(hkl) - F_{\text{cal}}(hkl)\right] \exp\left[i\varphi_{\text{cal}}(hkl)\right] \times \exp[-2\pi i(hx + ky + lz)]. \quad (8)$$

The difference Fourier presents the deformation density of the electron distribution around an atom from the ideal spherical distribution, because the atomic scattering factor is introduced from the Hartree–Fock approximation based on the spherical isolated-atom model. The deformation density interprets the valence electron or outer electron density such as the bonding electron or anisotropy of electron orbits.

7. Valence electrons of γ-SiO_2 under high pressure

We applied the new modification of the DAC for the structure analysis of rutile-type IVb oxides MO_2 ($P4_2/mnm$, $Z = 2$). These phases have received substantial attention because of their geophysical interest. Sinclair & Ringwood (1978) first described the single-crystal structure analysis of γ-SiO2. The rutile-type structures of transition elements have been studied by neutron diffraction Rietveld analysis (Bolzan *et al.*, 1997). The electron density distribution in γ-SiO_2 has been investigated by an X-ray diffraction study (Hill *et al.*, 1983; Spackman *et al.*, 1987; Yamanaka *et al.*, 2000). Crystal structure analyses under pressures up to 6 GPa (Sugiyama *et al.*, 1987), 16 GPa (Ross *et al.*, 1990) and 29.1 GPa (Yamanaka *et al.*, 2002) have been carried out. Molecular orbital calculations can provide important insight into the nature of the bonded interactions of materials. The bonding electrons observed from X-ray diffraction study are interpreted by the optimized pair potential and molecular orbital calculation (Svane & Antoncik, 1987; Mimaki *et al.*, 2000). The electron orbital overlapping and the bonding energy render the deformation of MO_6 octahedra of rutile-type structures from the bond character (Baur & Khan, 1971; Simunek *et al.*, 1993; Camargo *et al.*, 1996; Gibbs *et al.*, 1997, 1998). The structure change with pressure is characterized by the molecular orbital overlapping with the metal–metal interaction. However, electron density distribution has never been studied under pressure. Single-crystal structure analysis at 29.1 GPa (Yamanaka *et al.*, 2002) was carried out using a DAC with culet sizes of 400 μm, single-crystal diamond backing plates, a 20 μm × 20 μm × 20 μm single crystal, a 250 μm gasket hole, pressure-transmitting media of argon gas, and spring steel gasket pre-indented to 80 μm thickness.

The results of the structure refinements at various pressures are presented in Table 1, including the experimental conditions. The unit-cell volume at 29.1 GPa was reduced by as much as 9% compared with that at ambient pressure. The isothermal bulk modulus K_0 and K_0' were calculated from the volume change using the Birch-Murghanan equation of state (Table 2). The large K_0 value indicates that γ-SiO_2 is a noticeably hard crystal.

Interatomic distances are presented in Table 3. Notations of atoms are given in Fig. 3. Structure refinements from two sets of diffraction intensities obtained at ambient pressure and 29.1 GPa provide valence electron densities in the unit cell.

Table 1
Results of the structure refinements of γ-SiO_2 stishovite at various pressures.

Diffraction intensity measurement conditions and structure parameters, including atomic coordinates and temperature factors, are presented.

	Pressure				
	1 atm	5.23 GPa	9.26 GPa	12.3 GPa	29.1 GPa
Diffractometer	Rigaku AFC5		Rigaku AFC6R		Huber (512.1)
Wavelength	Mo $K\alpha$ (0.7107 Å)		Ag $K\alpha$ (0.5608 Å)		Synchrotron radiation (0.4077 Å)
Energy	150 kV, 50 mA		150 kV, 50 mA		8 GeV, 100 mA
Monochromator	Graphite (002)		Graphite (002)		Si(111) double crystal
Gasket	–		Spring steel		Spring steel
Pressure media	–		M:E:W† = 16:3:1		Ar
Scan mode	ω–2θ		φ-fix ω-scan		φ-fix ω-scan
Crystal size (μm)	50 × 60 × 80		40 × 40 × 60		20 × 20 × 40
2θ angle (°)	120	53	47	54	49
$\sin\theta/\lambda$	1.219	0.794	0.714	0.801	1.011
No. of observed and independent reflections	210, 126	81, 25	79, 25	82, 26	147, 57
a (Å)	4.1812 (1)	4.152 (1)	4.134 (1)	4.118 (2)	4.044 (6)
c (Å)	2.6662 (3)	2.6590 (8)	2.6540 (7)	2.649 (1)	2.619 (20)
c/a	0.6377	0.6404	0.6420	0.6433	0.6476
V (Å^3)	46.61	45.84	45.36	44.92	42.83
No. of reflections	126	25	25	26	36
$R(F)$‡	0.0253	0.0440	0.0312	0.0345	0.0330
$wR(F)$‡	0.0243	0.0234	0.0104	0.0227	0.0282
Si (000)	–	–	–	–	–
β_{11}	0.0045 (1)	0.0126 (27)	0.0055 (21)	0.0088 (20)	0.0035 (11)
β_{33}	0.0037 (5)	0.0261 (18)	0.0142 (12)	0.0103 (13)	0.0131 (13)
β_{12}	0.0002 (2)	0.0004 (21)	0.0021 (14)	0.0009 (12)	0.0019 (15)
O (xx0)	0.3063 (1)	0.3063 (20)	0.3056 (9)	0.3058 (19)	0.3039 (7)
β_{11}	0.0051 (2)	0.0075 (37)	0.0051 (29)	0.0104 (21)	0.0095 (13)
β_{33}	0.0036 (3)	0.0031 (17)	0.0090 (28)	0.0054 (18)	0.0074 (17)
β_{12}	−0.0009 (3)	0.0005 (35)	0.0009 (29)	0.0007 (35)	0.0004 (16)

† Pressure transmitting media are a mixture of methanol (M), ethanol (E) and water (W). ‡ $R(F) = \Sigma(||F_{obs}| - |F_{cal}||)/\Sigma|F_{obs}|$ and $wR(F) = \Sigma w(||F_{obs}| - |F_{cal}||)/\Sigma w|F_{obs}|$, where $w = 1/\sigma^2(|F_{obs}|)$.

In this study we applied a monopole refinement (Coppens *et al.*, 1979) instead of a multipole refinement. The number of reflections is limited in the case of a high-pressure diffraction study using a DAC. For the comparison between refinements at ambient conditions and at high pressure we performed a monopole refinement. Kirfel *et al.* (2001) reported the multipole analysis of stishovite at ambient conditions in a synchrotron single-crystal diffraction study.

In order to estimate the valence electron distributions from the κ-parameter, the reliability factor R was minimized with optimization of the variable κ-parameter and population parameter. The value of the κ-parameter for the O atom was 0.94 at ambient pressure and 1.11 at 29.1 GPa.

The Fourier transform of $f(s)$, including the population parameter (P) of the valence electrons in equation (3), defines the electron density $\rho(r)$ [equation (6)], and the spatial integration of $\rho(r)$ gives the effective charge of O atoms from equation (5). The κ-parameters of Si and O are presented in Table 4.

The electron distributions are more localized with increasing pressure. A smaller κ-parameter implies more bonding electrons and consequently a more covalent-bond nature. Our previous study of rutile-type MO_2 (M = Si, Ge and Sn) indicates that the κ-parameter of SiO_2 stishovite has a relatively strong covalent bond in comparison with the other two compounds (Yamanaka *et al.*, 2000).

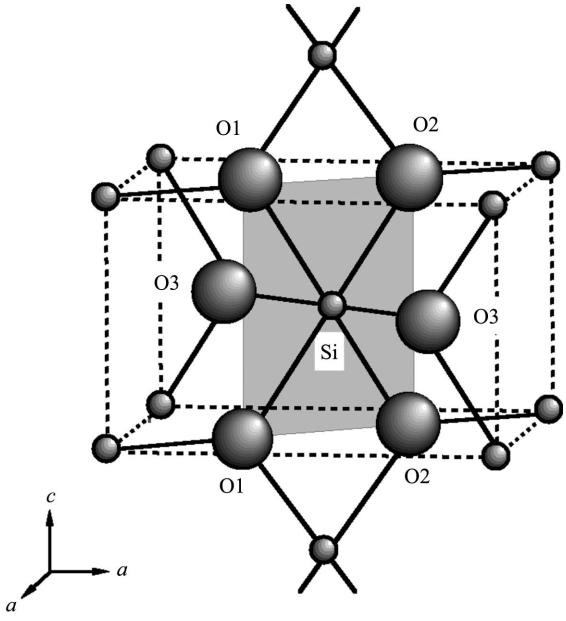

Figure 3
Structure of γ-SiO_2 stishovite. The shaded plane is the (110) plane, which is composed of equatorial oxygen atoms of O1 and O2 in the rutile structure.

Table 2
Isothermal bulk modulus of γ-SiO_2 stishovite.

	K_0 (GPa)	K_0'	P_{max} (GPa)	Data	Sample and remark
Our data	292 (13)	6 (fixed)	29.1	5	Single crystal
Andrault *et al.* (1998)	291	4.29	53.2	17	Powder and single†
Ross *et al.* (1990)	302 (5)	2.60 (0.8)	16	6	Single crystal
Ross *et al.* (1990)‡	287 (2	6 (fixed)			
Sugiyama *et al.* (1987)	313 (4)	6 (fixed)	6	9	Single crystal
Weidner *et al.* (1982)	306 (4)				Brilloin scattering

† The cell volume data are at pressures of 0.0001–15 GPa from Ross *et al.* (1990), at 24.6–49.4 GPa from Hemley *et al.* (1994) and at 48.1–53.2 GPa from Andrault *et al.* (1998). ‡ When K_0' is fixed to 6.

Table 3
SiO_6 octahedral volume and interatomic distances Si—O and O—O of γ-SiO_2 stishovite as a function of pressure.

Abbreviations of equatorial and apical bonds are indicated by eq and ap and those of shared and unshared edges by sh and unsh, respectively.

	Pressure				
	1 atm	5.23 GPa	9.26 GPa	12.3 GPa	29.1 GPa
Si—O (eq) (Å)	1.7559 (9)	1.750 (11)	1.748 (8)	1.742 (13)	1.724 (3)
Si—O (ap) (Å)	1.8111 (9)	1.798 (4)	1.784 (2)	1.781 (4)	1.738 (2)
ap/eq	1.0314	1.0274	1.0205	1.0223	1.0081
V (SiO_6) (Å^3)	7.374	7.266	7.178	7.134	6.806
O1—O2 (sh) (Å)	2.2906 (10)	2.277 (5)	2.275 (3)	2.262 (5)	2.242 (3)
O1—O1 (unsh) (Å)	2.6662 (3)	2.6590 (8)	2.6540 (7)	2.649 (1)	2.619 (2)
O1—O3 (Å)	2.5226 (4)	2.509 (10)	2.498 (10)	2.482 (17)	2.448 (2)
sh/unsh	0.8591	0.8563	0.8572	0.8539	0.8567

Table 4
κ-parameter, effective charge and dipole moment of Si in stishovite structure.

	Ambient conditions	29.1 GPa
κ-parameter of oxygen	0.94	1.11
Residual electron peak (position from Si)	0.86 Å	0.77 Å
Effective charge	+2.12 (8)	+2.26 (15)
Dipole moment	2.44	2.94

After refinement with the spherical-atom model, the deformations of electron distributions of γ-SiO_2 at ambient pressure and 29.1 GPa are disclosed by a difference Fourier map on the plane (110) as shown in Figs. 4(*a*) and 4(*b*), respectively. The map of γ-SiO_2 at ambient pressure shown in Fig. 4(*a*) is very similar to that of Hill *et al.* (1983) and Spackman *et al.* (1987). A positive peak of height 0.7 eV Å^{-3} is found at the almost middle position on the Si—O bond. Four positive residual densities around the cation are also recognized at 0.4 Å from the Si position. The residual electron peak position from the Si atomic position is 0.86 Å at ambient pressure and 0.77 Å at 29.1 GPa. The valence electron tends to be more localized at higher pressure. The localized density implies more ionic character under higher compression.

The residual electron densities shown in Fig. 4(*b*) are elongated in the direction of ⟨001⟩. This is because the sample orientation in the DAC did not provide all the reflections in full independent reciprocal space. Poor information on the high-order *l* reflections gives the elongated distribution.

Calculation of the density of state (DOS) of stishovite by Mimaki *et al.* (2000) reveals a significantly large amount of *d* electron density. The *d* orbital of sixfold-coordinated Si bridges the *p* orbital of O atoms. The shape of the residual electron density, indicating the bonding electron as shown in the difference Fourier map, represents the π bond instead of the σ bond. The non-spherical residual electron density around the cation site of Si is induced from the overlapping orbitals of the *d* electron of Si and the *p* electron of O, resulting in a $d-p-\pi$ bond. Hence, the noticeable residual electron density on the Si—O bond indicates a bonding electron. A large negative density in the bridging O—O bond plays a role in the hindrance of cation repulsion. The bonding electron distribution at 29.1 GPa is less noticeable compared with that at ambient conditions. This feature results from the observed κ-parameter and effective charge. The data indicate that SiO_2 stishovite becomes more ionic with increasing pressure.

Besides the bulk lattice deformation, the valence electron density distribution as a function of pressure has implications for understanding the structure stability and phase transformation mechanism. The electronic orbital overlapping causes deformation of octahedral coordination SiO_6 of the oxide structures and affects the character of the Si—O bond.

The ratio between shared and unshared edge distances of O—O has a strong relation with the interatomic repulsive force between two cations Si—Si and the degree of π bonding of Si—O. The ratio of shared/unshared edges changes with increasing pressure. The shared/unshared parameter is related to the ratio *c*/*a*.

The electron densities of states obtained by molecular orbital calculations (Mimaki *et al.*, 2000) are in good agreement with the results from X-ray photoelectron spectroscopy reported by Barret *et al.* (1991). The bonding electrons are related to the overlapped orbits of *s* and *p* electrons with *d* electrons. In order to investigate the bond character of rutile-type structures SiO_2, GeO_2, SnO_2 and PbO_2, we carried out molecular orbital calculations. A deformation electron density map at 30 GPa obtained from the molecular orbital calculations is shown in Fig. 5. The detailed procedure of the calculations is described in our previous paper (Mimaki *et al.*, 2000).

An apparent dipole moment (μ) may be experimentally determined by summation of the product of charge (q) and interatomic distance (r),

$$\mu_{obs} = \sum_{atom} q_i r_i, \qquad (9)$$

where q_i is the same value as the population P_i obtained from the present κ-refinement.

The apparent relative ionicity of rutile-type oxides can be expressed by μ_{obs}/μ_{ideal}, where μ_{ideal} is determined by the

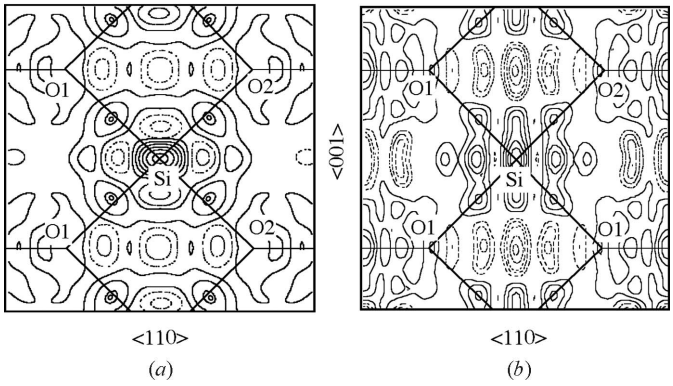

Figure 4
Difference Fourier map projected onto the (110) plane of γ-SiO_2 at (*a*) ambient pressure and (*b*) 29.1 GPa. Contours are at intervals of 0.2 e A^{-3} and positive and negative contours are expressed by solid and broken lines, respectively. Residual valence electron density clearly shows the distribution around the cations and the bonding electron distribution on the Si—O bond.

formal charge and interatomic distance. The results of the effective charge and dipole moments are presented in Table 4.

The deformation of octahedral coordination SiO_6 of the rutile-type structures can be induced from the bond character concerning the covalency. The *d* electron of cations increases the degree of the d—p—π bond in Si—O. The ratio between the shared and unshared edge distance of O—O has a strong relation with the interatomic repulsive force between the two cations Si—Si and the degree of the π bond of Si—O.

8. Pressure dependence of the electron density distribution of $FeTiO_3$ ilmenite by the maximum entropy method

The conventional difference Fourier analysis [equation (8)] encounters the problem of noise in the observed electron density distribution induced from the termination effect of the Fourier series. The diffraction angle using the DAC limits the number of $F(\mathbf{h})$ in the reciprocal space and lowers the quality of the structure refinement. Electron density distribution analysis by the maximum entropy method (MEM) conquers the problem and presents a much more reliable electron distribution. MEM statistically estimates the most reliable electron density distribution. The termination effect in the difference Fourier synthesis is ignored.

The ideal entropy (*S*) of MEM was introduced by Jaynes (1968) and the theory of MEM has been applied to structure analysis by Collins (1982), Sakata & Sato (1990), Sakata *et al.* (1992) and Yamamoto *et al.* (1996). *S* is represented by

$$S = -\sum_j \rho'(\mathbf{r}_j) \ln\left[\rho'(\mathbf{r}_j)/\tau'(\mathbf{r}_j)\right], \tag{10}$$

where electron density $\rho'(\mathbf{r}_j)$ and preliminary electron density $\tau'(\mathbf{r}_j)$ are

$$\rho'(\mathbf{r}_j) = \rho(\mathbf{r}_j)/\sum_j \rho(\mathbf{r}_j), \tag{11}$$

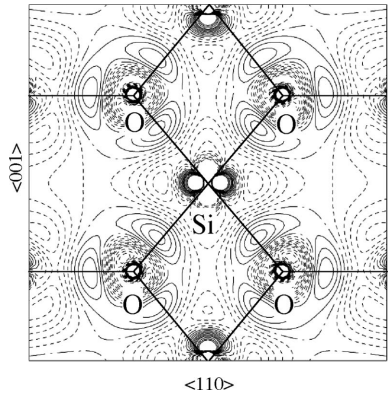

Figure 5
Deformation electron density map at 30 GPa obtained from molecular orbital calculation.

$$\tau'(\mathbf{r}_j) = \tau(\mathbf{r}_j)/\sum_j \tau(\mathbf{r}_j). \tag{12}$$

j is a minimum pick cell in the unit cell. $\tau(\mathbf{r}_j)$ indicates the electron density one cycle before the iteration of the least-squares calculation of $\rho(\mathbf{r})$. Fourier transform of the estimated $\tau(\mathbf{r}_j)$ provides $F_{\rm cal}(\mathbf{h})$,

$$F_{\rm cal}(\mathbf{h}) = V \sum_j \tau(\mathbf{r}_j) \exp(-2\pi i\, \mathbf{h}\cdot\mathbf{r}_j), \tag{13}$$

where *V* is the unit-cell volume. $\rho(\mathbf{r})$ is defined by

$$\rho(\mathbf{r}_j) = \tau(\mathbf{r}_j) \exp\left\{\frac{\lambda F_0}{N}\sum_{\mathbf{h}}\frac{1}{\sigma^2(\mathbf{h})}\left[F_{\rm obs}(\mathbf{h}) - F_{\rm cal}(\mathbf{h})\right] \times \exp\left(-2\pi i\, \mathbf{h}\cdot\mathbf{r}_j\right)\right\} \tag{14}$$

where *N* is the number of the observed $F_{\rm obs}(\mathbf{h})$, λ is Lagrange's undetermined coefficient and F_0 is the total number of electrons. The calculated $\rho(\mathbf{r}_j)$ replaces $\tau(\mathbf{r}_j)$ in the next cycle and calculates $F_{\rm cal}(\mathbf{h})$ again using equations (11) and (12). The least-squares calculation is repeated up to the cycle where $\sigma(\mathbf{r}_j)$ satisfies the condition $\rho(\mathbf{r}_j) \cong \tau(\mathbf{r}_j)$. Finally the calculation obtains the most reliable $F_{\rm mem}(\mathbf{h})$ and $\rho_{\rm MEM}(\mathbf{r}_j)$.

The detailed procedure of the MEM calculation based on $F_{\rm obs}(\mathbf{h})$ under high-pressure conditions will be presented elsewhere.

Much attention has been given to the structure transformations of oxides bearing transition elements from industrial uses, ferroelectrics, ferromagnetics and solid ionics. The electron density distribution of $Fe^{2+}Ti^{4+}O_3$ ilmenite ($R\bar{3}$, $Z = 6$) has been investigated as a function of pressure by an X-ray single-crystal diffraction study at high pressures up to 8.2 GPa using MEM. Fe^{2+} ($3d^6$) and Ti^{4+} ($3d^0$) cations across the shared face are alternatively located along the *c* axis. FeO_6 and TiO_6 octahedra are respectively located in a plane parallel to (001) and linked with adjacent octahedra with a shared edge. The cation–cation interactions in the structure have a significant meaning not only for the degree of disorder, such as corundum- or $LiNbO_3$-type structure, but also for physical properties and magnetism.

Diffraction intensity measurements at high pressures of 3.6, 5.3 and 8.2 GPa were made using a synchrotron radiation

Table 5
Result of the structure refinements of $FeTiO_3$ ilmenite at various pressures.

	Pressure			
	1 atm	3.6 GPa	5.3 GPa	8.2 GPa
$2\theta_{max}$ (°)	80	80	80	80
$\sin\theta/\lambda$ (Å^{-1})	0.91	0.90	0.90	0.90
a (Å)	5.08810 (4)	5.0678 (11)	5.0567 (13)	5.0398 (10)
c (Å)	14.0910 (10)	13.9956 (9)	13.8892 (10)	13.7968 (12)
c/a	2.769	2.762	2.747	2.738
V (Å^3)	315.93 (5)	310.40 (13)	307.57 (16)	303.49 (12)
No. of reflections used	408	215	214	200
R (%)	1.81	3.29	3.56	4.19
wR (%)	2.99	4.40	4.71	5.78
Fe (00z) (Å^2)				
z	0.355430 (9)	0.35570 (5)	0.35568 (5)	0.35611 (7)
B_{eq}	0.457 (1)	0.390 (9)	0.36 (1)	0.22 (1)
Ti (00z) (Å^2)				
z	0.146429 (9)	0.14641 (5)	0.14641 (6)	0.14695 (8)
B_{eq}	0.352 (1)	0.31 (1)	0.28 (1)	0.29 (1)
O (xyz) (Å^2)				
x	0.31717 (9)	0.3169 (5)	0.3169 (5)	0.3185 (8)
y	0.02351 (9)	0.0233 (5)	0.0232 (5)	0.0233 (7)
z	0.24498 (3)	0.24538 (9)	0.24533 (10)	0.24600 (15)
B_{eq}	0.48 (1)	0.33 (11)	0.30 (11)	0.35 (15)
Fe (Å^2)				
$U_{11}U_{22}$	0.00582 (3)	0.0050 (2)	0.0046 (3)	0.0021 (3)
U_{33}	0.005732 (1)	0.004860 (3)	0.004362 (3)	0.004136 (5)
U_{12}	$U_{11}/2$	$U_{11}/2$	$U_{11}/2$	$U_{11}/2$
$U_{13}U_{23}$	0	0	0	0
Ti (Å^2)				
$U_{11}U_{22}$	0.00433 (3)	0.0037 (3)	0.0033 (3)	0.0040 (4)
U_{33}	0.004709 (1)	0.004430 (4)	0.004123 (4)	0.002976 (6)
U_{12}	$U_{11}/2$	$U_{11}/2$	$U_{11}/2$	$U_{11}/2$
$U_{13}U_{23}$	0	0	0	0
O (Å^2)				
U_{11}	0.0050 (1)	0.0037 (10)	0.0027 (10)	0.0043 (16)
U_{22}	0.0057 (1)	0.0043 (10)	0.0043 (11)	0.0051 (14)
U_{33}	0.006784 (1)	0.004844 (7)	0.005017 (7)	0.003313 (10)
U_{12}	0.00209 (9)	0.0023 (9)	0.0021 (9)	0.0018 (14
U_{13}	0.000221 (8)	0.00055 (8)	0.00028 (8)	0.00025 (12)
U_{23}	0.001462 (8)	0.00039 (8)	0.00024 (9)	0.00025 (12)
G_{iso} ($\times10^{-4}$)	0.180	0.198	0.197	0.196

wavelength of 0.61907 Å at BL-10A, KEK, Japan, with the above-mentioned DAC. The structure parameters including the anisotropic thermal parameters of $FeTiO_3$ at various pressures are presented in Table 5. The cation positions move in the direction of the c axis and approach the center of FeO_6 and TiO_6 with increasing pressure. The regularity of the TiO_6 octahedra is enhanced at higher pressure. Bond distances of Fe—O, Ti—O, O—O octahedral edges, selected bond angles and FeO_6 and TiO_6 volumes are presented as a function of pressure in Table 6. All oxygen atoms O1 to O9 (indicated in Fig. 6) occupy a crystallographically equivalent position. These octahedra have a pair of three equivalent bond distances, M—O (sh face) and M—O (unsh face) (M = Fe and Ti). M—O (sh face) and M—O (unsh face) bond lengths are presented as a function of pressure. The bond angle ∠O—M—O (sh face) corresponds to the O1—O2—O3 shared face, and ∠O—M—O (unsh face) to the O4—O5—O6 face in AO_6 and the O7—O8—O9 face in BO_6 opposite to the vacant space.

Table 6
Selected interatomic distances and bond angles of $FeTiO_3$.

	Pressure				
	1 atm	3.6 GPa	5.3 GPa	8.2 GPa	β†
Fe—O_{sh} ×3	2.2017 (6)	2.185 (2)	2.178 (3)	2.170 (4)	1.8 (2)
Fe—O_{unsh} ×3	2.0795 (6)	2.064 (3)	2.059 (3)	2.041 (4)	2.2 (2)
⟨Fe—O⟩	2.1406	2.125	2.119	2.106	2.0 (2)
Ti—O_{sh} ×3	2.0867 (6)	2.077 (3)	2.069 (3)	2.066 (5)	1.3 (2)
Ti—O_{unsh} ×3	1.8745 (6)	1.868 (3)	1.863 (3)	1.859 (4)	1.0 (1)
⟨Ti—O⟩	1.9806	1.973	1.967	1.963	1.1 (2)
Fe—Ti	2.9450 (3)	2.9210 (10)	2.9065 (11)	2.8858 (15)	2.47 (7)
Fe—Fe_1‡	3.0029 (2)	2.9918 (7)	2.9850 (8)	2.9769 (8)	1.07 (4)
Fe—Fe_2	4.0743 (3)	4.0275 (9)	4.0091 (10)	3.9704 (14)	3.09 (6)
Ti—Ti_1	2.9925 (2)	2.9800 (7)	2.9732 (8)	2.9602 (8)	1.31 (6)
Ti—Ti_2	4.1267 (4)	4.0860 (10)	4.0671 (12)	4.0548 (16)	2.18 (3)
O—O_1§	2.6975 (9)	2.686 (5)	2.680 (5)	2.684 (7)	0.7 (3)
O—O_2	3.2184 (9)	3.205 (5)	3.198 (5)	3.180 (8)	1.4 (2)
O—O_3	3.0539 (5)	3.020 (2)	3.009 (2)	2.981 (3)	2.9 (1)
O—O_4	3.0073 (7)	2.975 (3)	2.965 (3)	2.930 (5)	3.1 (2)
O—O_5	2.9210 (6)	2.911 (3)	2.976 (3)	2.886 (4)	1.4 (3)
O—O_6	2.6041 (6)	2.593 (2)	2.582 (3)	2.586 (4)	0.9 (4)
O—O_7	2.8851 (6)	2.872 (3)	2.860 (3)	2.857 (5)	1.3 (2)
O—Fe—O_1¶	75.55 (2)	75.84 (10)	75.94 (10)	76.40 (15)	
O—Fe—O_2	89.20 (2)	88.83 (8)	88.78 (8)	88.15 (11)	
O—Fe—O_3	90.97 (2)	90.54 (10)	90.46 (10)	90.08 (14)	
O—Fe—O_4	101.40 (3)	101.75 (10)	101.86 (11)	102.34 (15)	
O—Ti—O_1	80.54 (2)	80.58 (10)	80.72 (11)	81.01 (15)	
O—Ti—O_2	82.01 (2)	82.02 (8)	81.90 (9)	82.23 (13)	
O—Ti—O_3	93.34 (2)	93.30 (9)	93.12 (9)	93.27 (13)	
O—Ti—O_4	102.36 (3)	102.28 (11)	102.46 (11)	101.90 (15)	
Fe—O—Ti	86.70 (2)	86.49 (11)	86.33 (11)	85.84 (16)	

† β ($\times10^{-3}$ GPa^{-1}): coefficients of compressibility. ‡ Metal–metal distances are indicated as follows: 1, across shared edge between adjacent metal sites; 2, across vacant octahedral position, along ⟨001⟩. § Oxygen–oxygen distances are indicated as follows: 1, Fe—Ti shared face; 2, Fe site, face opposite the shared face; 3, Fe site, shared edge; 4, Fe site, unshared edge; 5, Ti site, face opposite the shared face; 6, Ti site, shared edge; 7, Ti site, unshared edge. ¶ Oxygen–metal–oxygen angles are indicated as follows: 1: shared face; 2: shared edge; 3: unshared edge; 4: unshared face.

Three M—O bonds (sh face) of the FeO_6 and TiO_6 octahedra are longer than those of the M—O (unsh face). The longer M—O (sh face) bonds are more shortened under pressure than the shorter M—O (unsh face). Therefore the cation shifts toward the center of the octahedron. The compressions of the Ti—O bond lengths are smaller than those of Fe—O. The shared edge of the octahedron, O—O (sh edge), is less influenced by compression than O—O (unsh edge). With increasing pressure, M—O (sh face) of both octahedra is more compressed than M—O (unsh face). The tendency is more noticeable in FeO_6 octahedra than in TiO_6 octahedra.

In comparison with the difference Fourier synthesis, MEM calculation using $F_{mem}(\mathbf{h}) - F_{cal}(\mathbf{h})$ gives a much more precise electron distribution that indicates the deformation electron density. Figs. 7(*a*) and 7(*b*) show the Fourier synthesis and the difference Fourier map, respectively, on the basis of the 0.0001 GPa data set.

The $\sigma(\mathbf{h})$ of the error in $F_{obs}(\mathbf{h})$ in equation (13) of the MEM calculation empirically applied the parameters of a = 1.5–4.5 and b = 1.0–1.5 in $\sigma(\mathbf{h}) = a(\sin\theta/\lambda) + b$. The best conditions for the least squares of MEM using each data set at various pressures is summarized in Table 7. Lagrange's undetermined

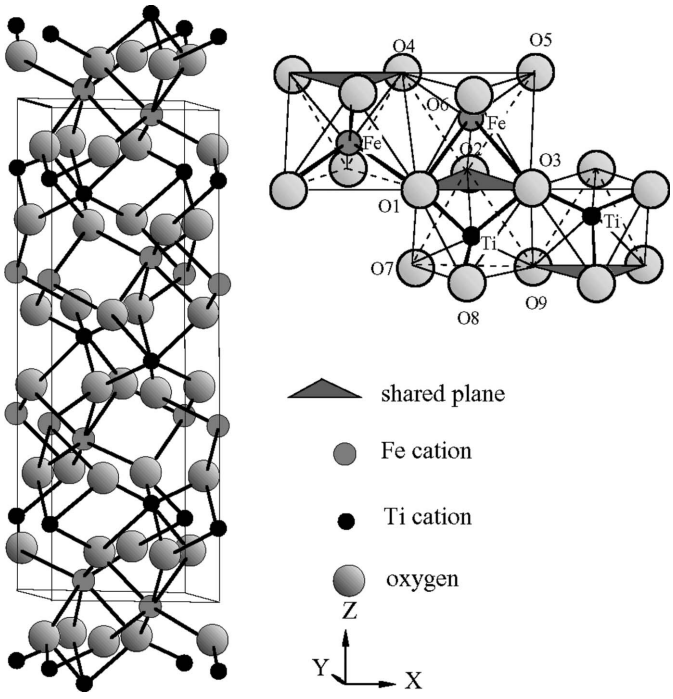

Figure 6
Structure of $FeTiO_3$ and configuration of FeO_6 and TiO_6 octahedra.

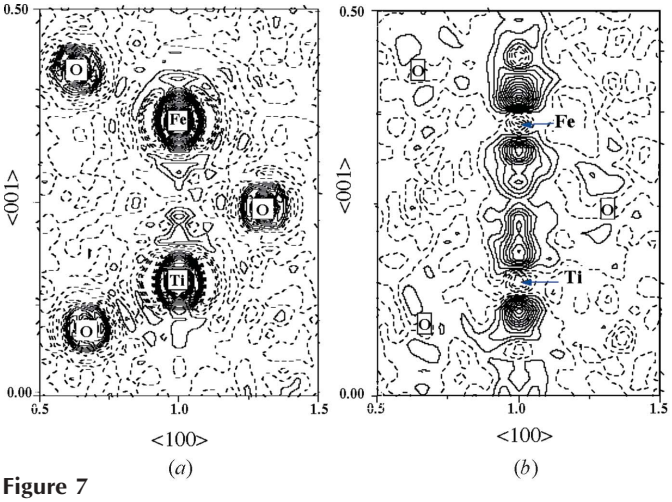

Figure 7
Electron density distribution of $FeTiO_3$ observed by (*a*) Fourier synthesis and (*b*) residual electron density by difference Fourier ($F_{obs} - F_{cal}$) on the (010) plane at 0.0001 GPa. The $\sin\theta/\lambda < 1.22$ data set is used for the calculation. The contour lines are drawn from 8.0 to 328 e Å^{-3} with 80 e Å^{-3} intervals for (*a*) and from 0.2 to 4.0 e Å^{-3} with 0.2 e Å^{-3} intervals for (*b*).

Table 7
Parameters for the MEM calculation of $FeTiO_3$ at various pressures.

	Pressure				
	1 atm†	1 atm	3.6 GPa	5.3 GPa	8.2 GPa
No. of reflections	933	408	215	214	200
Maximum 2θ (°)	120	80	80	80	80
Maximum $\sin\theta/\lambda$	1.22	0.91	0.90	0.90	0.90
a (Å)‡	1.0	1.0	1.2	1.2	1.5
b (Å)	1.5	1.5	3.5	4.0	4.5
λ ($\times 10^{-5}$) (Å)	0.2	0.5	0.3	0.35	0.35
No. of MEM cycles	863	285	801	779	879
R-factor (%)	6.33	4.08	5.13	5.63	6.36

† Data without using DAC. ‡ $\sigma(\mathbf{h}) = a(\sin\theta/\lambda) + b$.

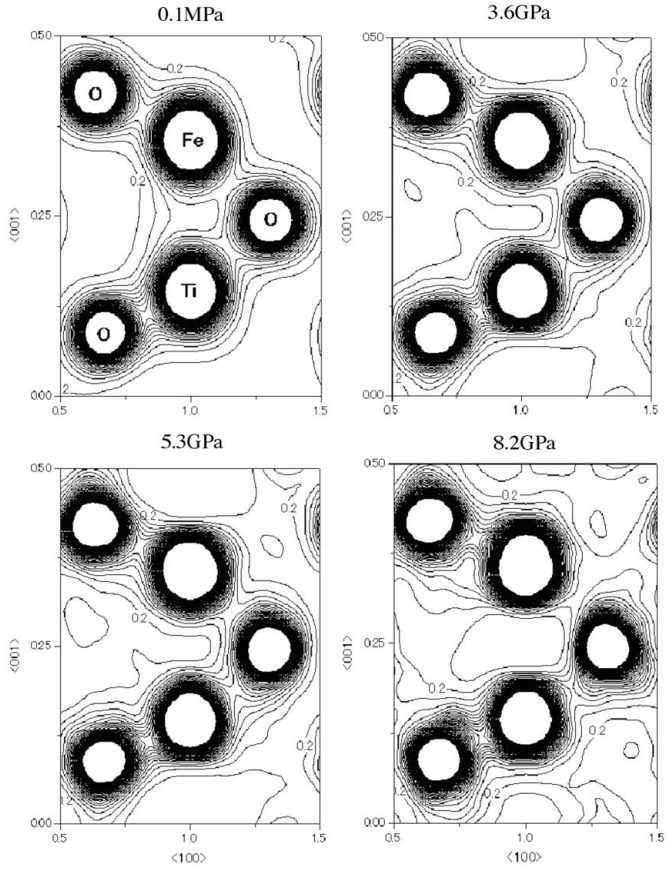

Figure 8
Electron density maps on the (010) plane calculated with MEM at 0.0001, 3.6, 5.3 and 8.2 GPa. The $\sin\theta/\lambda < 0.90$ data sets are used for both calculations. The contour lines are drawn from 0.2 to 4.0 e Å^{-3} with 0.2 e Å^{-3} intervals.

coefficient λ in equation (14) is also presented in the table. We tested the accuracy of the electron density analysis corresponding to the number of $F_{obs}(\mathbf{h})$ related to the observed reciprocal space in $\sin\theta/\lambda$, because the diffraction angle using the DAC is limited to up to 70° in 2θ as shown in Fig. 2. The test proves that the electron density distributions using $F_{obs}(\mathbf{h})$ within $2\theta < 60$, 80, 100 and 120° are not so greatly different, but the localization of the electron distribution is more clearly indicated by the data sets from a larger region of reciprocal space.

The MEM analysis reveals the valence electron densities of Fe and Ti. Fig. 8 shows the electron distribution on the (010) plane at 0.0001, 3.6, 5.3 and 8.2 GPa. At ambient pressure the electron density distributions around the Fe^{2+} ($3d^6$) and Ti^{4+} ($3d^0$) cations are not spherical, but are elongated along the direction of the *c*-axis owing to the *d*-electron orbital. The compression affects the Coulomb potential in $M-O$ (M = Fe, Ti) bonds and the repulsive force is enhanced under high-pressure conditions. The electron densities on the Fe—O (sh) and Ti—O (sh) bonds are more increased with pressure than

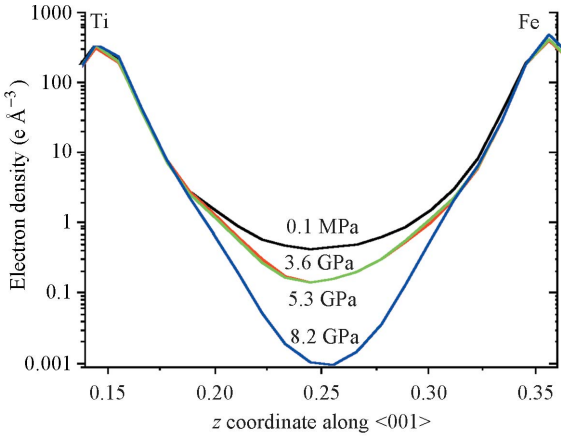

Figure 9
Radial distribution of electron density between Fe and Ti at various pressures. The abscissa indicates the z coordination of Fe and Ti position along ⟨001⟩.

those on the Fe—O (unsh) and Ti—O (unsh) bonds, respectively. The former two densities indicate a greater increase in the bonding electron on their bonds with compression than the latter two. On the other hand, the compression reduces the bonding electron on both the Fe—O (unsh) and Ti—O (unsh) bonds. The electron density between the Fe^{2+} ($3d^6$) and Ti^{4+} ($3d^0$) cations across the shared face becomes smaller with increasing pressure.

The localization of the valence electron around the cation is enhanced under higher pressure. The MEM calculations prove that the pressure dependence of the electron radial distribution obviously shows more localization of electrons around cations with increasing pressure, as shown in Fig. 9. This is clarified by the radial distribution since the electron density between the Fe^{2+} and Ti^{4+} cations across the shared face becomes smaller with increasing pressure. This is because the repulsion of d electrons between the two cations is enlarged with the external compression. However, the electron conductivity measurement using a polycrystalline sample, which will be reported elsewhere, reveals increasing conductivity at higher pressure. The electron distribution between Fe and Ti along ⟨001⟩ becomes lower with pressure. Hence neither charge transfer nor electron hopping in $FeTiO_3$ is possible under pressure.

9. Summary

X-ray diffraction study gives the electron density distributions including valence electrons and bonding electrons. Charge density analysis based on the diffraction intensities provides a view of the effective charge of the ions and the dipole moment.

The charge distribution reveals a significant admixture of covalency in the chemical bonds of rutile-type SiO_2, and the appropriate charge state of the cations turns out to be far from a formal charge of Si^{4+} electron configuration. The significant d-electron population indicates some degree of non-sphericity of valence electron distribution around Si. The difference Fourier map of γ-SiO_2 (Figs. 4*a* and 4*b*) reveals an apparently non-spherical electron distribution around Si.

Compression of $FeTiO_3$ reduces the bonding electron on both Fe—O (unsh) and Ti—O (unsh) bonds as shown in the MEM map (Fig. 8). The electron density between Fe^{2+} ($3d^6$) and Ti^{4+} ($3d^0$) cations across the shared face becomes smaller with increasing pressure. In both cases of γ-SiO_2 and $FeTiO_3$ the valence electron localization around the cation position is more enhanced under higher pressure.

As seen Tables 1 and 5, the isotropic thermal distribution parameters B_{iso} of γ-SiO_2 and $FeTiO_3$ are reduced with increasing pressure. This is because the atomic thermal vibration is considerably restrained by the lattice compression from the external pressure P_{ext}.

References

Andrault, D., Fiquet, G., Guyot, F. & Hanfland, M. (1998). *Science*, **282**, 720–724.
Barret, T. L., Mohsenian, M. & Chen, L. M. (1991). *Appl. Surf. Sci.* **51**, 71–87.
Baur, W. H. & Khan, A. A. (1971). *Acta Cryst.* B**27**, 2133–2139.
Bolzan, A. A., Fong, C., Kennedy, B. J. & Howard, C. J. (1997). *Acta Cryst.* B**53**, 373–380.
Camargo, A. C., Iguarada, J. A., Beltrain, A., Lhustar, R., Lango, E. & Anders, J. (1996). *Chem. Phys.* **212**, 381–391.
Collins, D. M. (1982). *Nature (London)*, **298**, 49–51.
Coppens, P., Guru Row, T. N., Leung, P., Stevens, E. D., Becker, P. J. & Yang, W. (1979). *Acta Cryst.* A**35**, 63–72.
Gibbs, G. V., Boisen, M. B., Hill, F. C., Tamada, O. & Downs, R. T. (1998). *Phys. Chem. Miner.* **25**, 574–584.
Gibbs, G. V., Hill, F. C. & Boisen, M. B. Jr (1997). *Phys. Chem. Miner.* **24**, 167–178.
Hemley, R. J., Prewitt, C. T. & Kingma, K. J. (1994). *Reviews of Mineralogy*, edited by P. Heaney, G. V. Gibbs and C. T. Prewitt, pp. 41–81. Washington, DC: Mineralogical Society of America.
Hill, R. J., Newton, M. D. & Gibbs, G. V. (1983). *J. Solid State Chem.* **47**, 185–200.
International Tables for X-ray Crystallography (1974). Vol. III. Birmingham: Kynoch Press.
Jaynes, E. T. (1968). *IEEE Trans. Syst. Sci. Cybern.* SSC**4**, 227.
Kim-Zajonz, J., Werner, S. & Schulz, H. (1998). *Z. Kristallogr.* **214**, 331–336.
Kirfel, A., Krane, H. G., Blaha, P., Schwarz, K. & Lippmann, T. (2001). *Acta Cryst.* A**57**, 663–677.
Mao, H. K., Bell, P. M., Shaner, J. W. & Steinberg, D. J. (1978). *J. Appl. Phys.* **49**, 3276–3283.
Mimaki, J., Tsuchiya, T. & Yamanaka, T. (2000). *Z. Kristallogr.* **215**, 419–423.
Ross, N. L., Shu, J. F., Hazen, R. M. & Gasparik, T. (1990). *Am. Mineral.* **75**, 739–747.
Sakata, M. & Sato, M. (1990). *Acta Cryst.* A**46**, 263–270.
Sakata, M., Uno, T., Takata, M. & Moriet, R. (1992). *Acta Cryst.* B**48**, 591–598.
Sasaki, S. & Tsukimura, K. (1987). *J. Phys. Soc. Jpn*, **56**, 437–440.
Simunek, A., Vackar, J. & Wiech, G. (1993). *J. Phys. Condens. Matter*, **5**, 867–874.
Sinclair, W. W. & Ringwood, A. E. (1978). *Nature (London)*, **272**, 714–715.
Spackman, M. A., Hill, R. J. & Gibbs, G. V. (1987). *Phys. Chem. Miner.* **14**, 139–150.
Sugiyama, M., Endo, S. & Koto, K. (1987). *Mineral. J.* **13**, 455–466.
Svane, A. & Antoncik, E. (1987). *J. Phys. Chem. Solids*, **48**, 171–180.
Wal, R. J. van der & Stewart, R. F. (1984). *Acta Cryst.* A**40**, 587–593.

Weidner, D. J., Bass, J. D., Ringwood, A. E. & Sinclair, W. (1982). *J. Geophys. Res.* **87**, 4740–4746.
Yamamoto, K., Takahashi, Y., Ohshima, K., Okamura, F. P. & Yukino, K. (1996). *Acta Cryst.* A**52**, 606–613.
Yamanaka, T., Fukuda, T., Hattori, T. & Sumiya, H. (2001). *Rev. Sci. Instrum.* **72**, 1458–1462.
Yamanaka, T., Fukuda, T. & Tsuchiya, J. (2002). *Phys. Chem. Miner.* **29**, 633–641.
Yamanaka, T., Kurashima, R. & Mimki, J. (2000). *Z. Kristallogr.* **215**, 424–428.
Zhang, L., Ahsbahs, H. & Kutoglu, A. (1998). *Phys. Chem. Miner.* **25**, 301–307.